Pd/Ag Nanoparticles Prepared in Ionic Liquids as Model Catalysts for the Hydrogenation of Diphenylacetylene

Georgios Uzunidis and Silke Behrens*

Supporting Information available online

Dedicated to Prof. Dr. Thomas Hirth on the occasion of his 60th birthday

The preparation of bimetallic Pd/Ag-based model catalysts is addressed to study the promotional effects of Ag doping in the liquid-phase semi-hydrogenation of diphenylacetylene. The precursor concept is employed where colloidal bimetallic Pd/Ag nanoparticles are initially synthesized and then used as well-defined building units for catalyst preparation. This approach allows for tuning the composition of the nanoparticles independently with the two metals co-localized to a fine extent. Size and composition of the nanoparticles are preserved after immobilizing them on a carbon support.

1 Introduction

The selective catalytic hydrogenation of acetylenic compounds has not only attracted a lot of interest in fundamental research but is also extensively used in fine organic synthesis and various industrial processes [1, 2]. The purification of ethylene from steam cracking, for example, is a large-scale, industrial process in which impurities in acetylene are removed by selective hydrogenation [3, 4]. Even traces of acetylenic compounds poison the metallocene catalyst during downstream ethylene polymerization [1, 5]. The partial hydrogenation of substituted alkynes to *cis*-alkenes in the liquid phase is also a key step in the production of vitamins, fragrances, polymers and agrochemicals [6–8]. The most commonly used metals are nickel, palladium, and platinum [9–14]. Palladium-based heterogeneous catalysts, in particular, reveal high activity, recyclability, and sustainability compared to homogeneous and stoichiometric reagents [15]. One major challenge in the Pd-catalyzed partial hydrogenation of alkynes is to prevent over-hydrogenation of the alkenes to the corresponding alkanes and/or the formation of high molecular weight oligomeric species from unsaturated moieties. Alkene selectivity may be improved to some degree by optimizing the reaction conditions, but this requires substrate-specific fine tuning. A common way to increase selectivity is the modification of palladium with a second metal [13]. The Lindlar

catalyst, where palladium is modified by addition of lead, is a prototypic example with high selectivity to *cis*-alkenes under mild reaction conditions [13, 15–18]. Economic aspects associated with the high Pd loading and the toxicity of lead together with stricter environmental regulations have driven the search for new alternatives [15, 19]. The selectivity to alkenes is also significantly improved for binary bimetallic Pd-M particles (e.g., with M = Cu [20], Ag [21–23], Au [24], Zn [6], Ga [25, 26], In [27–29], Sn [30], or Bi [31]) or even ternary Pd-based phases (such as Pd-Bi-Se [32] or Pd-Ga-Sn [33, 34]). In addition, non-precious, binary alloys (Ni-Fe or Ni-Ga) [35, 36], intermetallic compounds ($Al_{13}Fe_4$) [37], transition metal-free Zintl phases ($BaGa_2$), or non-precious, ternary phases (Cu-Ni-Fe) [38] have been reported as catalysts for semi-hydrogenation of alkynes in the gas or liquid phase.

The use of bimetallic Pd-Ag catalysts in the gas-phase semi-hydrogenation of acetylene was initially reported by Dow Chemical Co in 1957 and implemented in commercial application in the front-end acetylene semi-hydrogenation

Dr. Georgios Uzunidis, Prof. Dr. rer. nat. Silke Behrens
silke.behrens@kit.edu
Karlsruhe Institute of Technology, Institute of Catalysis Research and Technology, Hermann-von-Helmholtz-Platz 1, 76344 Eggenstein-Leopoldshafen, Germany.

by Chevron Philips and Süd-Chemie in the early 1980s [4]. The high selectivity of Pd-Ag catalysts is associated with a number of characteristics of their specific geometric and electronic structure [39]. While silver is not active in the hydrogenation reaction, it prevents the formation of multi-atomic Pd_n ($n \geq 2$) ensembles. The geometric isolation of active Pd centers (site isolation effect) facilitates ethylene desorption and decreases its over-hydrogenation to the corresponding alkane [40]. Moreover, electronic charge transfer effects between silver and palladium further reduce the heat of adsorption of ethylene on the Pd centers [41, 42]. DFT calculations by Studt et al. [9] showed that the addition of silver reduces the energy barrier for alkene desorption and favors ethylene desorption, increasing selectivity in the reaction [43]. In addition, modification with Ag is known to hinder the formation of sub-surface hydrogen and PdH_x phases typically leading to undesirable over-hydrogenation to the alkane [44].

However, research on such systems is limited by the poor availability of bimetallic catalytic systems with homogeneous distribution of size, morphology and chemical composition. Heterogeneous catalysts produced by conventional impregnation and (co)precipitation procedures are often poorly defined and reveal non-uniform particle sizes and shapes with random distribution of active and promotor phases [21, 39, 45–47]. Thus, it is often difficult to really attribute the catalytic properties to compositional changes of the catalyst. For the manufacturing of model catalysts in the liquid-phase semi-hydrogenation of diphenylacetylene (DPA), we employ the precursor concept as a promising strategy to address the promotional effects of Ag doping on palladium catalysts [48]. In this context, colloidal bimetallic Pd/Ag nanoparticles (NPs) were initially synthesized and then used as well-defined building units for catalyst preparation. By this procedure, the composition of the NPs is tuned independently with the two metals co-localized to a fine extent. Size and composition of the NPs are preserved during their successive immobilization on a carbon support. In general, the catalytic properties of bimetallic NPs are very sensitive to the elemental composition and the atomic arrangement. Pd forms alloys with Ag over the whole compositional range; the formation of ordered intermetallic structures is not observed [49]. Alloyed Pd/Ag NPs in a broad compositional range have been obtained, e.g., by solvothermal synthesis using oleylamine as a solvent/reductant, oleylamine/oleic acid in 1-octadecene or an emulsion-assisted, ternary ethylene glycol/oleylamine/oleic acid mixture [50–52]. Here, we make use of the beneficial properties of ionic liquids (ILs) for synthesizing well-defined Pd/Ag NPs in a similar size range but with different molar Pd/Ag ratio. The NPs are characterized by transmission electron microscopy (TEM), optical emission spectroscopy with inductively coupled plasma (ICP-OES) and powder X-ray diffraction analysis (XRD). We show that alloying with Ag increases the selectivity and yield of *cis*-stilbene (CST) in the liquid-phase hydrogenation of DPA.

2 Experimental

2.1 Materials

Chemicals were purchased from Air Liquide[A], Acros Organics[B], Aldrich[C], Degussa[D], Merck[E], Sigma-Aldrich[F], and VWR Chemicals[G], i.e., argon (99.9999 %)[A], 1-butyl-3-methylimidazolium bis(trifluoromethylsulfonyl)-imide [BMIm][NTf$_2$] (>98.0 %)[E], cyclohexane (anhydrous, 99.9 %)[F], diphenylacetylene (98 %)[C], 1,2-diphenylethane (>99 %)[G], ethanol (99.8 %)[G], *n*-hexan (anhydrous, 95.0 %)[F], oleylamine (70 %)[F], oleic acid (90 %)[F], palladium(II)acetate (Pd(ac)$_2$) (99.99 %)[B], palladium(II)acetylacetonate (Pd(acac)$_2$) (35 % Pd)[B], silver(I)acetate (Ag(OAc)) (99.99 %)[F], silver bis(trifluoromethylsulfonyl)-imide (AgNTf$_2$) (97 %)[F], *cis*-stilbene (96 %)[F], *trans*-stilbene (96 %)[F], tetrabutylammonium borohydride ([NBu$_4$][BH$_4$]) (98 %)[F], tetrahydrofuran (THF) (anhydrous, >99,9 %)[F], Vulcan XC-72 Carbon Black (CB)[D].

2.2 NP Synthesis in ILs

NP synthesis was carried out under an argon atmosphere in the glovebox. Pd(acac)$_2$ and AgNTf$_2$ (for details see Tab. 1) were dissolved in [BMIm][NTf$_2$] (1 or 2 mL depending on the experiment) by stirring at 50 °C for 20 min. [NBu$_4$][BH$_4$] was dissolved in [BMIm][NTf$_2$] (1 or 2 mL

Table 1. Summary of experimental parameters for the synthesis of monometallic Pd reference NPs and alloyed Pd/Ag NPs in [BMIm][NTf$_2$].

Entry	Name	Ionic liquid	Pd precursor Pd(acac)$_2$	Ag precursor AgNTf$_2$	Reducing agent TBABH$_4$ [mg]	CB [mg]	Metal loading [wt %]
1	Pd	[BMPyrr][NTf$_2$][a]	30.6 mg, 100 µmol	–	100	500	2.0
2	Pd$_3$Ag	[BMIm][NTf$_2$][a]	22.8 mg, 75 µmol	9.7 mg, 25 µmol	100	450	1.7
3	PdAg	[BMIm][NTf$_2$][b]	30.6 mg, 100 µmol	38.8 mg, 100 µmol	200	2×500	1.5
4	PdAg$_2$	[BMIm][NTf$_2$][b]	20.4 mg, 67.5 µmol	51.2 mg, 132.5 µmol	200	2×500	2.0

a) 1 mL [NBu$_4$][BH$_4$] solution and 1 mL metal precursor solution in the IL were combined. b) 2 mL [NBu$_4$][BH$_4$] solution and 2 mL metal precursor solution in the IL were combined.

depending on the experiment) in a separate Schlenk flask (10 mL) by stirring at room temperature for 20 min. Both solutions were heated to 80 °C in an aluminum socket and stirred at 80 °C for 5 min. Then, the solution of the metal precursors was rapidly injected into the vigorously stirring [NBu$_4$][BH$_4$] solution. NP formation is indicated by the formation of a black dispersion. The reaction mixture is stirred for additional 20 min at 80 °C. The bimetallic NPs were extracted in n-hexane by adding a coordinating ligand. For this purpose, oleylamine (i.e., 1 mL oleylamine in 2 mL n-hexane) was quickly added to the rapidly stirring NP IL sol (2 mL). The mixture was stirred overnight. Afterwards, the organic and IL phase were separated, and the top layer transferred to a centrifuge tube (50 mL). Ethanol (30 mL) was added, which leads to the precipitation of the NPs. The NPs were isolated by centrifugation (2–20 min, 2935–7197 rcf). The NPs were purified by washing three times with n-hexane/ethanol (1:30). The NPs were stored after dispersing in n-hexane (10 mL) as a black organosol.

For catalyst preparation, the NPs were immobilized on carbon black (Vulcan XC-72). Therefore, the carbon support was well suspended in n-hexane by stirring and sonicating for 30 min. The amount of carbon black was calculated to reach a metal loading of the final catalyst of approx. 2 wt % (for details see Tab. 1). The NP dispersion in n-hexane was added dropwise to the stirring suspension of the support. Afterwards, the mixture was further stirred while sonicating for another 30 min to ensure complete precipitation on the carbon support. The carbon-supported NPs were isolated by centrifugation (2–20 min, 2935–7197 rcf) and subsequently washed with n-hexane/ethanol, ethanol and THF (3–5 times). The catalyst was dried in vacuum at 30 °C and received as a black powder.

2.3 Characterization

X-ray diffraction (XRD) analysis of the carbon-supported NP was carried out using a PANalytical X'Pert Pro instrument using a Bragg-Brentano geometry with Cu-Kα radiation (1.54060 Å) and a Ni filter. The diffractograms were recorded from 20° to 100° (2θ) over a period lasting two times 2 h at room temperature. The reflections were compared to reference data reported in the International Centre for Diffraction Data (ICDD) database (Ag (ICDD 98-060-4629), Pd (ICDD 98-004-1517)). The Pd and Ag content of the NPs and the metal loading of the catalysts were determined by ICP-OES (Agilent 735-ES instrument). For electron microscopy studies, the catalysts were mounted on carbon-coated Ni grids by applying a droplet of the catalyst powders suspended in n-hexane. The grids were then dried in vacuum (10^{-2} mbar) for several hours. The samples were analyzed with an FEI Tecnai F20 ST TEM (operating voltage 200 kV), which was equipped with a field emission gun and EDAX EDS X-ray spectrometer and by SEM on a Zeiss GeminiSEM500, equipped with a Schottky-type ther-

mal field emission cathode. From TEM images, a number n of particles > 200 was measured to calculate mean particle sizes and to establish size histograms (see Fig. 3) with number of particles $n = 217$ for Pd NPs, $n = 292$ for Pd$_3$Ag NPs, $n = 280$ for PdAg NPs and $n = 309$ for PdAg$_2$ NPs. Elemental mapping by STEM-EDX was performed on an FEI Osiris ChemiStem (200 kV) at the Laboratory for Electron Microscopy. Due to overlapping of the L lines, the K elemental lines of Pd and Ag were used for quantification. However, the intensity of the K lines was very low, which contributes to an increased experimental error.
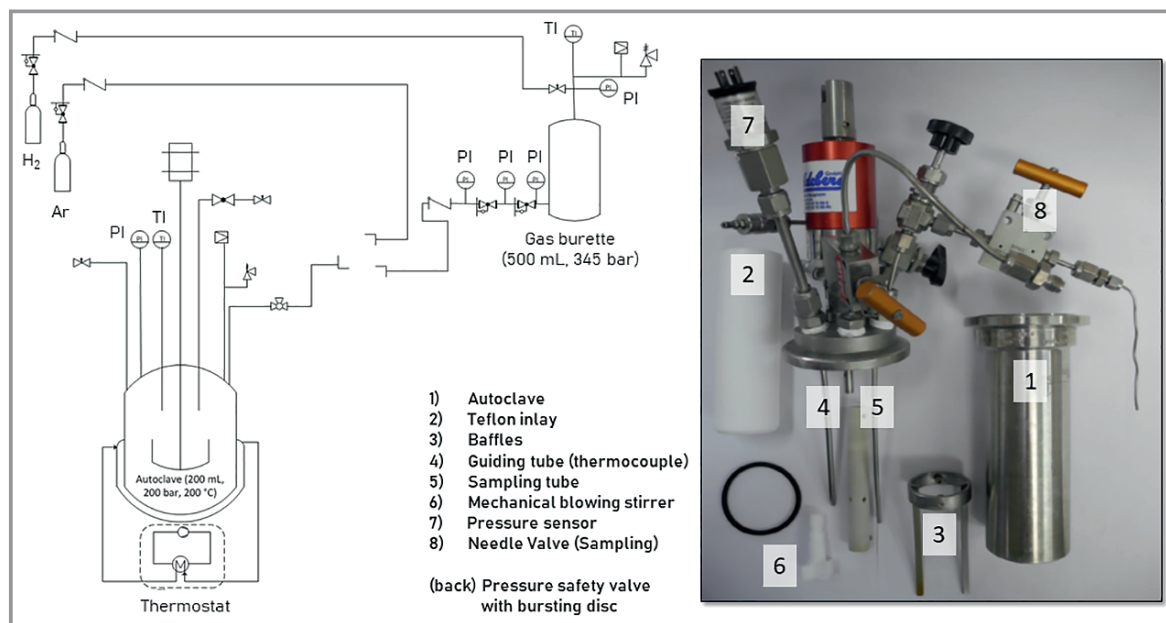
2.4 Catalytic Tests

The catalytic tests were carried out in a semi-continuous batch reactor (Fig. 1). The stainless-steel autoclave was equipped with a PTFE Teflon® inlay, a mechanical blowing stirrer (Teflon®) and baffles (stainless steel). A high-pressure gas burette (Parr Instruments, 500 mL, stainless steel) with electronic pressure sensor and thermocouple (both connected to a data logger (Agilent 34970A)) was used for continuous hydrogen supply. A sampling tube allowed monitoring of reaction kinetics by taking aliquots of liquid samples during catalytic tests. For catalytic tests, the autoclave reactor was loaded in the glovebox with a suspension of the carbon-supported NP catalysts in a solution of DPA (1 g, 5.60 mmol) in cyclohexane (20 mL) [26 mg (Pd NPs, entry 1), 32 mg (Pd$_3$Ag NPs, entry 2), 35 mg (PdAg NPs, entry 3), 25 mg (PdAg$_2$ NPs, entry 47]. Then, the reaction temperature was raised to 35 °C while stirring (1100 rpm). At 35° C the reaction was started by hydrogen initiation into the reactor. During catalytic experiments, the hydrogen pressure was kept constant at 8 bar. Liquid samples were taken at regular intervals and analyzed by gas chromatography (GC) (Agilent 7890B) using a Stabilwax-DA column (Agilent Technology, 30 m × 0.25 mm, 0.25 µm film thickness).

Concentrations were determined from peak areas after calibration with standard DPA, CST, TST and DPE solutions (regression coefficients: $r_{DPA} = 0.9997$, $r_{CST} = 0.9998$, $r_{TST} = 0.9996$, $r_{DPE} = 0.9998$). The results were used to determine DPA conversion X_{DPA}, product yield Y (Y_{CST}, Y_{TST}, Y_{DPE}) and product selectivity S (S_{CST}, S_{TST}, S_{DPE}). The DPA conversion X_{DPA}, product selectivities (S_{CST} [%], S_{TST} [%], S_{DPE} [%]) and product yields (Y_{CST} [%], Y_{TST} [%], Y_{DPE} [%]) were calculated according to the following equations:

$$X_{DPA,t} = 100 - \frac{n(DPA, t)}{n(DPA, t) + n(CST) + n(TST) + n(DPE)} 10^2 \quad (1)$$

$$S_{(CST, TST, or DPE)} = \frac{n(Product(CST, \ TST, \ or \ DPE))}{n(CST) + n(TST) + n(DPE)} 10^2 \quad (2)$$

Figure 1. Schematic representation and photo of the laboratory reactor used for catalytic tests in the semi-hydrogenation of DPA.

$$Y_{(\mathrm{CST,\,TST,\,DPE})} = S_{(\mathrm{CST,\,TST,\,DPE})}\, X_{\mathrm{DPA}}\, 10^{-2} \qquad (3)$$

where t is the reaction time (min), $n_{\mathrm{DPA},t}$ is the DPA amount at time t (mol), and $X_{DPA,t}$ is the conversion of DPA at time t (%).

3 Results and Discussion

In a first step, bimetallic Pd/Ag-based NPs were synthesized by chemical reduction of the metal salts (Fig. 2). An ionic liquid (IL) (i.e., [BMIm][NTf$_2$]) was employed as a reaction medium. Due to their unique, tailor-made properties (e.g., low vapor pressure, high polarity, and wide electrochemical stability window), room-temperature ILs represent interesting reaction media for NP synthesis [53, 54]. In ILs, NP nucleation and growth processes may be controlled by weakly coordinating anions and cations, which also act as (electro)steric stabilizers against NP agglomeration [30, 55–58].

The dissolution of all reactants and a homogeneous nucleation process were a prerequisite for the formation of homogeneously alloyed Pd/Ag particles. Otherwise, only segregated Pd and Ag particles were obtained, as indicated by XRD analysis. Some of the common Ag salts (such as AgOAc and AgNO$_3$) and Pd(OAc)$_2$ are not soluble in [BMIm][NTf$_2$]. Therefore, AgNTf$_2$ and Pd(acac)$_2$ were chosen as metal precursors for NP synthesis forming a homogeneous solution in [BMIm][NTf$_2$] at 50 °C. Na[BH$_4$], which is often used as reducing agent in NP synthesis, is also not soluble in [BMIm][NTf$_2$]. Therefore, [NBu$_4$][BH$_4$] was used here as a reducing agent that can be dissolved in
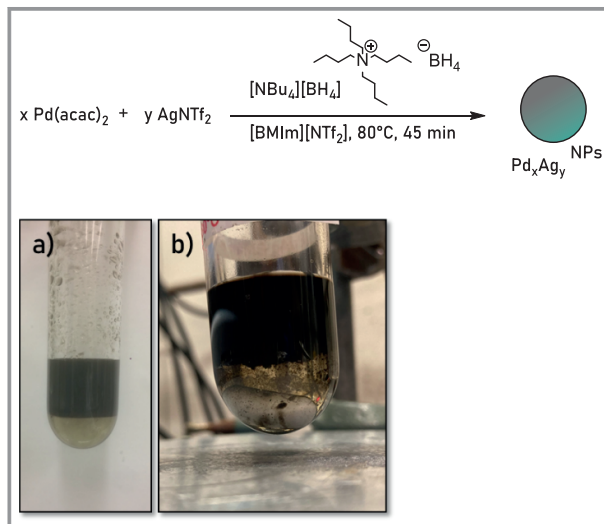
Figure 2. Reaction scheme of the synthesis of alloyed Pd/Ag NPs by reduction of the metal precursors in [BMIm][NTf$_2$] with [NBu$_4$][BH$_4$] at 80 °C. After the reaction in the IL, the Pd/Ag NPs are extracted from the IL (lower pale yellow phase) to *n*-hexane (upper black phase) using oleylamine: a) PdAg NPs (entry 3), b) PdAg2 NPs (entry 4).

[BMIm][NTf$_2$]. The Pd/Ag precursor ratio was decreased from 3:1 over 1:1 to 1:2, and the effects on particle size and composition were investigated (Tab. 2).

The reaction was carried out at 80 °C, which reduces IL viscosity and allows rapid (co)reduction of the precursors. In addition, monometallic Pd particles were prepared in an analogous procedure, which served as reference in catalytic studies. The bimetallic Pd/Ag particles were received as

Table 2. Summary of analytical results of the NPs from synthesis in [BMIm][NTf$_2$] at 80 °C with different precursor ratios.

Entry	Catalyst	Molar Pd/Ag ratio		Metal loading [wt %]	NP size [nm][a]	Crystallite size [nm][b]	Bragg angle (2θ) / hkl
		Initial	NPs[c]				
1	Pd NPs@CB	100:0	100:0	2.0	2.7 ± 0.4	–	40.1° / 111
2	Pd$_3$Ag NPs@CB	75:25	75:25	1.7	4 ± 1	3	39.0° / 111
3	PdAg NPs@CB	50:50	49:51	1.5	5 ± 1	3	38.8° / 111
4	PdAg$_2$ NPs@CB	33:66	35:65	2.0	5 ± 2	4	38.5° / 111

a) The NP size was determined by counting at least 200 particles from TEM images. b) The crystallite size was calculated according to the Scherrer equation using the 111 reflection of unsupported NPs. c) The molar ratio of the NP was determined by ICP-OES.

black dispersion in the IL. For catalyst preparation, the NPs were isolated from the IL and transferred to *n*-hexane using oleylamine as a ligand (Fig. 2). To elucidate the effect of Ag alloying, organic ligands are either removed by thermal or chemical treatment or the same type of ligand must be used for all catalysts. Notably, thermal or chemical treatment may lead to segregation, oxidation, or leaching selectively for one of the metals changing either their atomic arrangement or even the overall metal composition. Therefore, we use the same synthetic protocol with oleylamine for phase transfer to prepare both the monometallic Pd reference NPs and the bimetallic Pd/Ag NPs with tunable composition. The as-isolated NPs were then dispersed over the carbon support. To achieve carbon-supported NPs with a metal loading of approx. 2 wt %, the NP dispersion in *n*-hexane was added dropwise to the carbon support suspended in *n*-hexane (Tab. 1). The carbon-supported monometallic Pd and bimetallic Pd/Ag NPs were characterized by ICP-OES, TEM and XRD analysis.

The particle size and size distribution of the Pd/Ag NPs was determined by statistical measurement from a large number *n* of NPs ($n > 200$) using transmission electron microscopy (TEM) imaging (Fig. 3, Tab. 2). The Pd and Pd/Ag NPs are small with spherical shape and dispersed over the carbon support. Among the supported NPs, the monometallic Pd NPs (Fig. 3a) reveal the smallest diameter (2.7 ± 0.4 nm). The bimetallic Pd/Ag NPs (entries 2–4) are in a similar size range (4 to 5 nm). The mean diameter only slightly increases with increasing Ag content from 4 (± 1) nm (Pd$_3$Ag NPs) to 5 (± 1) nm (PdAg NPs) and 5 (± 2) nm (PdAg$_2$ NPs) (Tab. 2).

This is important with respect to catalytic investigations on the effect of Ag alloying because DPA semi-hydrogenation is known to reveal an antipathetic structure sensitivity (i.e., the turnover frequency increases with particle size) [59]. In addition, the atomic arrangement of the two metals in the NP may vary with size [60]. The molar Pd/Ag ratio of the NPs was determined by ICP-OES analysis and is in good agreement of the employed ratios of the metal precursors.

EDX elemental mapping further demonstrates the uniform metal loading and homogenous NP distribution on the carbon support (see Figs. S2–S5 in the Supporting Information). Fig. 4 shows the results of XRD analysis of the supported, bimetallic Pd/Ag NPs as compared to their monometallic Pd NP counterparts and the carbon support (Vulcan XC-72). The XRD patterns revealed very broad reflections of low intensity, which is characteristic for small NPs. The XRD diagrams of the carbon-supported, bimetallic Ag/Pd particles show three reflections at 38–39°, 43°, and 79° (2θ). Reflections at 43° and 79° (2θ) can be attributed to the carbon support. The 111 reflection of the bimetallic Pd/Ag NPs is at 38–40° (2θ) and thus, between the 111 reflection of the Ag (ICDD 98-060-4629) and Pd (ICDD 98-004-1517) reference at 38.2° and 40.1° (2θ), respectively (Tab. 2). With increasing Ag content of the NPs, the 111 reflection shifts to lower Bragg angles. In general, a shift of the reflections to lower Bragg angles is characteristic for an increase in lattice constants by incorporation of Ag in the face centered cubic (fcc) Pd lattice and the formation of solid solution-type, bimetallic NPs. The crystallite sizes determined by the Scherrer equation are in the range of 3–4 nm (entries 1–4) and in good agreement with the particle sizes determined by TEM imaging. Due to the small size of the monometallic Pd reference NPs (entry 1), the XRD pattern only reveals reflections of very low intensity, which partially overlapped with the reflections of the carbon support and thus, crystallite sizes could not be determined. This observation is also in good agreement with the mean diameter of the Pd particles of 2.7 (± 0.4) nm as determined by TEM analysis.

The STEM-EDX maps (Fig. 5) show co-localized Pd and Ag with similar distribution, further indicating the formation of Pd/Ag alloy NPs. The mean composition measured over approx. 20 NPs was 72 (± 18) at % Pd and 23 (± 18) at % Ag for Pd$_3$Ag NPs, 48 (± 18) at % Pd and 52 (± 18) at % Ag for PdAg NPs, and 45 (± 23) at % Pd and 55 (± 23) at % Ag for PdAg$_2$ NPs, respectively. Some variation in elemental composition between individual NPs in addition to the increased elemental error for EDX quantification due to low signal intensity of the K elemental lines may have contributed to the high standard deviation. It should be noted that STEM-EDX maps of PdAg$_2$ NPs reveal the presence of some additional Pd-rich, alloyed NPs
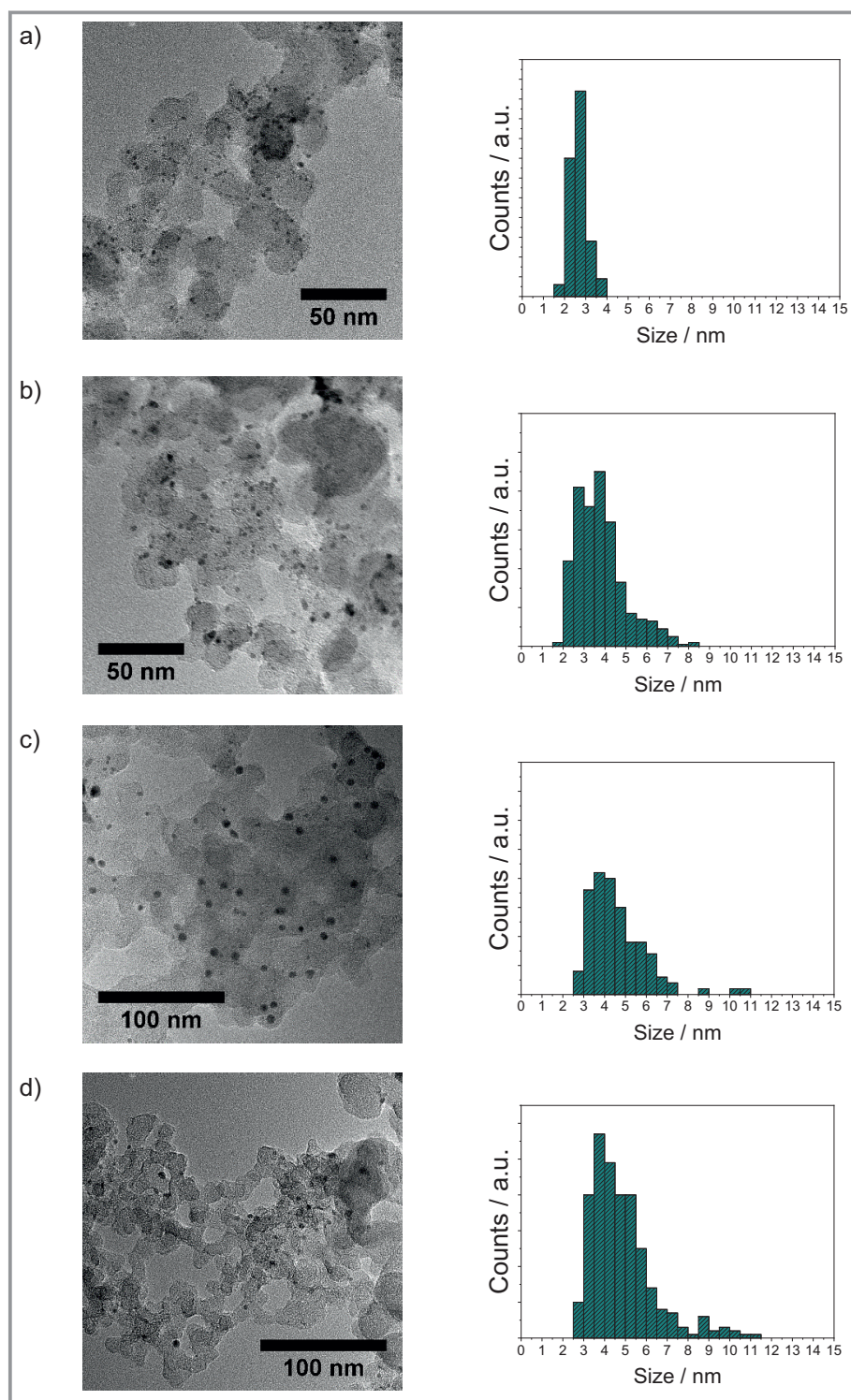
Figure 3. Representative TEM images and size histograms of the monometallic Pd NP reference and the carbon-supported, bimetallic Pd/Ag NPs obtained by synthesis in [BMIm][NTf$_2$] at 80 °C: a) Pd NPs, b) Pd$_3$Ag NPs, c) PdAg NPs, and d) PdAg$_2$ NPs.

The catalytic properties of the carbon-supported Pd/Ag NPs were tested in the liquid-phase semi-hydrogenation of DPA and compared to the monometallic Pd NP reference. Fig. 6 displays possible reaction pathways, intermediates and products in the hydrogenation of DPA. DPA hydrogenation involves the semi-hydrogenation to *cis*-stilbene (CST) or *trans*-stilbene (TST) and their hydrogen-mediated isomerization. Derivatives of CST and TST are used as dyes, liquid crystals, optical brighteners, OLEDs, or in the production of food additives [61]. However, the selective hydrogenation of substituted carbon-carbon triple bonds may be challenging, as adsorption heats of reactants and intermediates are often similar. Therefore, the DPA hydrogenation process is also associated with irreversible over-hydrogenation to 1,2-diphenylethane (DPE), which lowers the yield of the *cis*- and *trans*-alkenes.

In general, it has been suggested that an absence of the PdH$_x$ phase and the formation of isolated Pd centers increase the alkene selectivity in this reaction. For example, Rassolov et al. have reported that the formation of PdH$_x$ phases is completely suppressed in Al$_2$O$_3$-supported Pd/Ag alloys with equimolar stoichiometry [62].

However, the formation of stable, isolated Pd centers occurred only above a Pd/Ag stoichiometry of 1:2. In our study, carbon-supported Pd/Ag NP catalysts with a Pd/Ag ratio of 3:1, 1:1 and 1:2 were investigated in the hydrogenation of DPA and compared to the monometallic Pd reference catalyst. The hydrogenation was carried out in a semi-continuous batch reactor with continuous H$_2$ feed (8 bar) at
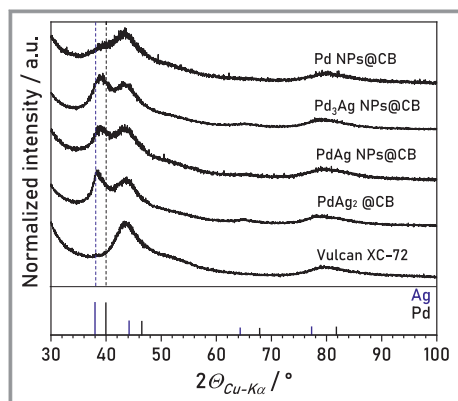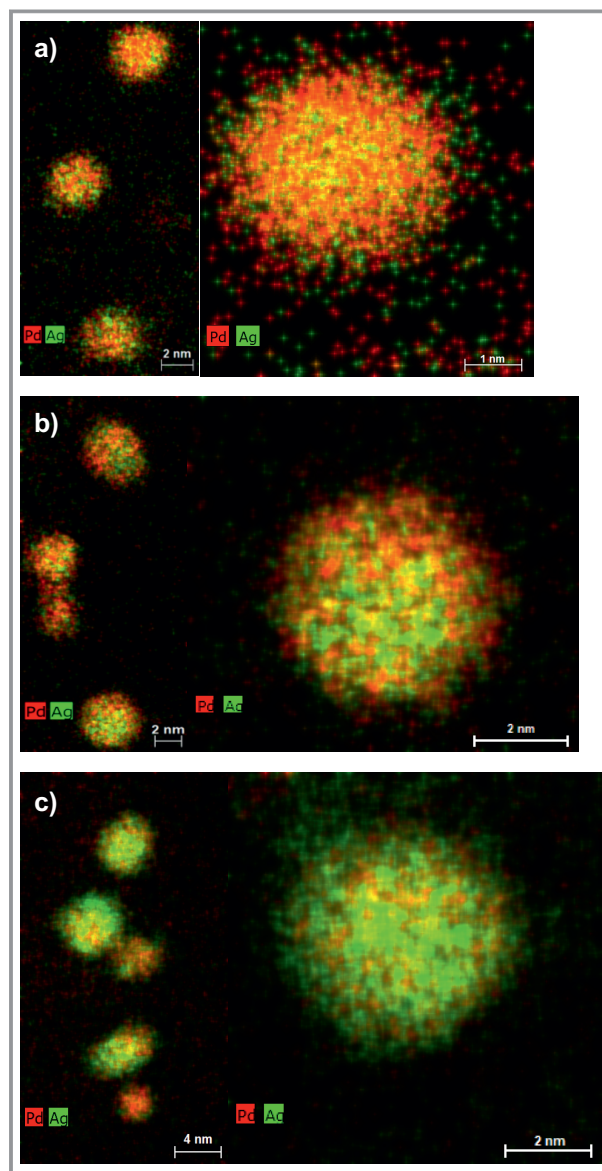
of smaller size. These results are in good agreement with the elemental composition determined by ICP-OES analysis.

35 °C in cyclohexane. The ratio of DPA to total metal was kept constant for all catalytic tests. The catalytic performance is summarized in Tab. 3 with the maximum in CST

Figure 4. XRD patterns of carbon-supported, monometallic Pd NPs and alloyed Pd/Ag NPs with different molar Pd/Ag ratios (references: Ag (blue, ICDD 98-060-4629), Pd (black, ICDD 98-004-1517)).


Figure 5. Elemental maps obtained from STEM-EDX spectrum of the carbon-supported, bimetallic Pd/Ag NPs: a) Pd_3Ag NPs, b) PdAg NPs, and c) $PdAg_2$ NPs.

selectivity (S_{max}(CST)) and CST yield (Y_{max}(CST)) and the CST selectivity (S_{DPA50}(CST) and the CST yield (Y_{DPA50}(CST)) for 50 % DPA conversion. Figs. 7 and 8 show the time dependencies of the product selectivity and yield for Pd/Ag NP catalysts with different Pd/Ag ratio, respectively. The evolution of the CST concentration and CST yield profiles suggests a consecutive reaction mechanism, where DPA hydrogenation leads to the formation of the alkene, which is then further hydrogenated to the alkane in the second step.

The Pd NP reference catalyst and the Pd-rich Pd_3Ag NPs revealed 100 % DPA conversion after approx. 20 min of reaction (entries 1 and 2) while DPA conversion was 100 % after 30 min of reaction (entries 3 and 4) for the PdAg and the Ag-rich $PdAg_2$ NPs. In all cases, DPA hydrogenation proceeded rapidly, but the selectivity and product yield as a function of reaction time strongly depended on the catalyst composition. For all alloyed Pd/Ag NPs, the CST selectivity (S_{max}(CST), S_{DPA50}(CST)) and the CST yield (Y_{max}(CST), Y_{DPA50}(CST)) were increased with respect to the monometallic Pd reference NPs. For example, the Y_{max}(CST) was 11 and 36 %, which was reached quickly after 7 and 10 min for the Pd NP reference and the Pd-rich Pd_3Ag NPs, respec-

Table 3. Maximum CST yield (Y_{max}(CST)) and selectivity (S_{max}(CST)) as well as selectivity (S_{DAP50}(CST)) and yield (Y_{DAP50}(CST)) at 50 % DPA conversion in the selective hydrogenation of DPA over bimetallic Pd/Ag NP and monometallic Pd catalysts.

Entry	Catalyst	Y (CST) [%][a]		S (CST) [%][a]	
		Y_{max}	Y_{DPA50}	S_{max}	S_{DPA50}
14	Pd-NP @CB	11 (7 min)	11	30 (5 min)	25
15	Pd_3Ag-NP @CB	36 (10 min)	30	50 (5 min)	50
16	PdAg-NP @CB	65 (20 min)	42	82 (15 min)	80
17	$PdAg_2$-NP @CB	76 (22 min)	44	86 (15 min)	86

a) The time at which the maximum CST yield and selectivity was reached is given in brackets.
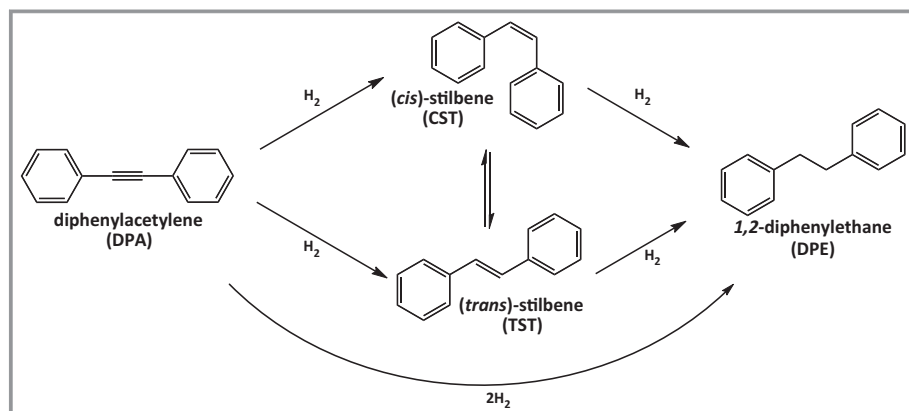
Figure 6. Reaction network for the hydrogenation of diphenyl-acetylene (DPA).

tively (Tab. 3, Fig. 8a, 8b). S_{max}(CST) was also increased from 30 % to 50 % after alloying the Pd NPs with Ag in Pd$_3$Ag NPs. However, the alkene was also rapidly over-hydrogenated to DPE with 100 % DPE selectivity and yield already after approx. 20 min of reaction. With further increase of the Ag content in PdAg NPs or in PdAg$_2$-NPs, S_{max}(CST) increased to to 82 and 86 % (Fig. 7c, 7d) and Y_{max}(CST) to 65 and 76 % (Fig. 8c, 8d), respectively.

However, the effect of the Ag-rich (PdAg$_2$) with respect to the equimolar (PdAg) NP composition on CST selectivity was less pronounced and CST selectivity was high in both cases for conversions up to approximately 95 % (Fig. 9). At

around 95 % DPA conversion, the CST selectivity of the PdAg and PdAg$_2$ NPs steeply decreased whereas DPE selectivity and yield increased (Fig. 8).

In general, the superior catalytic performance of bimetallic Pd/Ag catalysts in the semi-hydrogenation of acetylenic compounds has been attributed to the isolation of active Pd sites on the surface by the Ag addition, resulting in weakly π-bonded acetylene, and to a reduction in the hydrogen amount incorporated into the catalyst. However, atomic arrangements in NPs can differ from those of ideal bulk alloys and exhibit more complicated structures. In general, the surface of bimetallic Pd/Ag NPs is significantly enriched
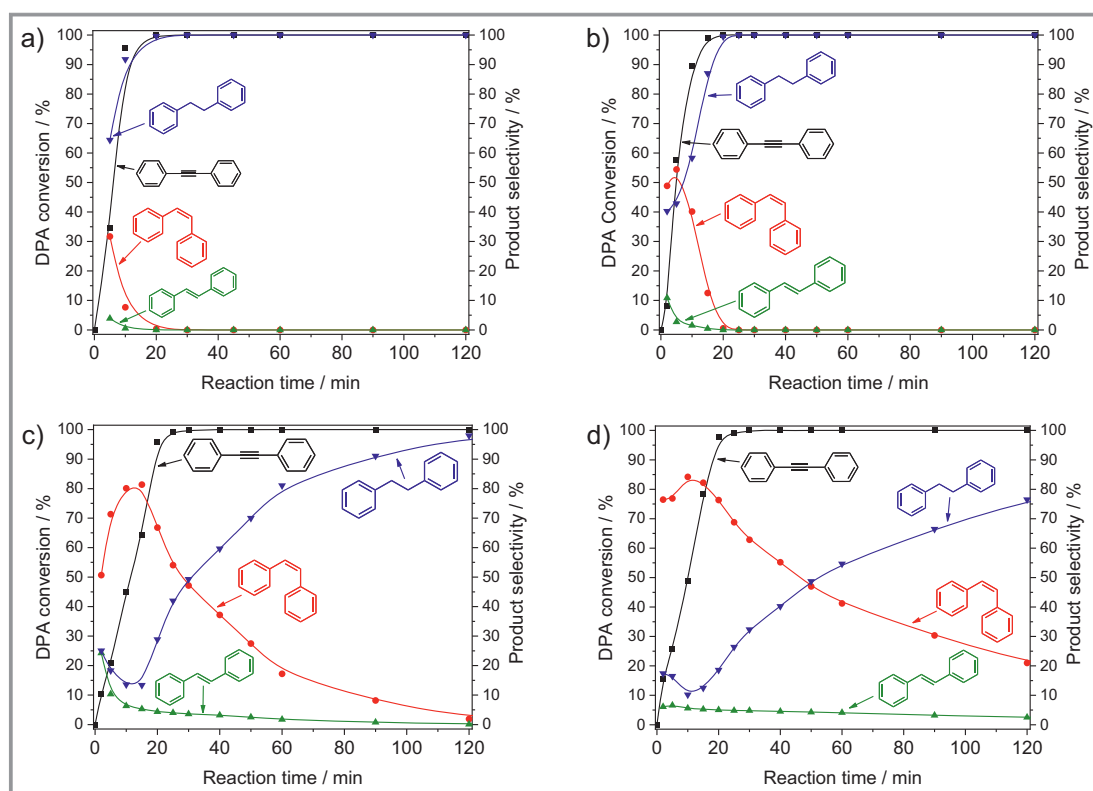

Figure 7. Time course of the reaction mixture composition during DPA hydrogenation over carbon-supported Pd and Pd/Ag NP catalysts: a) Pd reference NPs, b) Pd$_3$Ag NPs, c) PdAg NPs, and d) PdAg$_2$ NPs. Reaction conditions: 5 µmol total metal on Vulcan CX-72, 5.6 mmol DPA, 20 mL cyclohexane, 8 bar H$_2$, 35 °C, 1110 rpm.
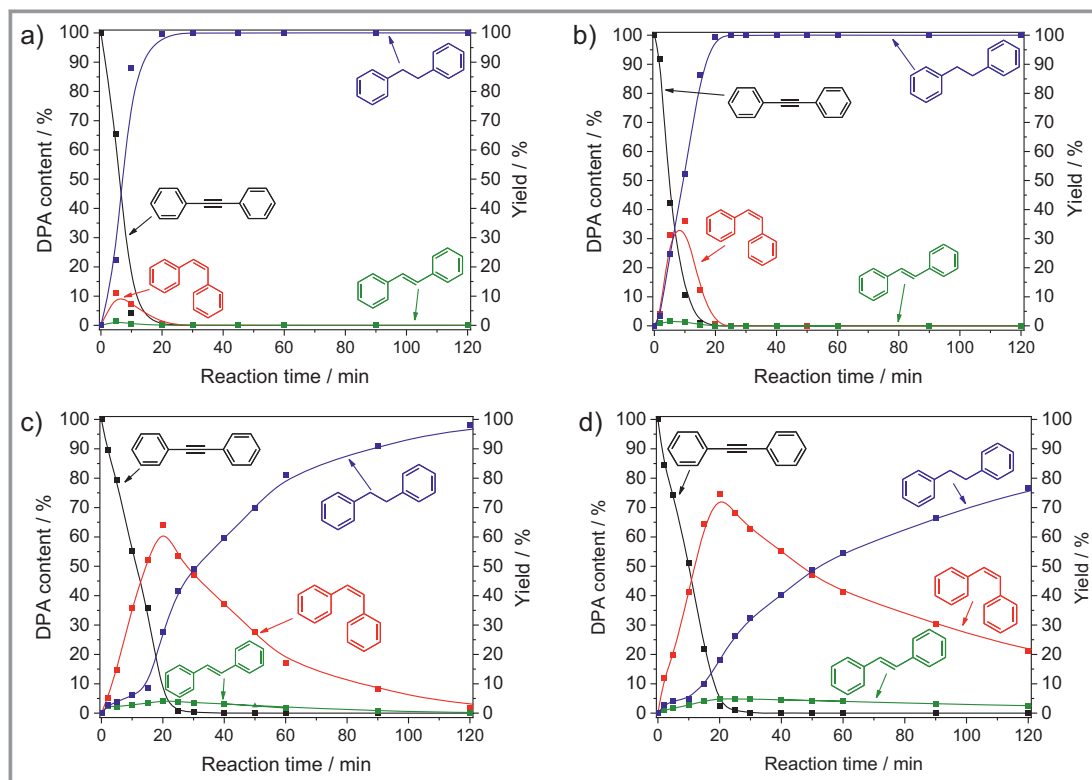
Figure 8. Time course of the product yield during DPA hydrogenation over carbon-supported monometallic Pd and alloyed Pd/Ag NP catalysts: a) Pd reference NPs, b) Pd_3Ag NPs, c) PdAg NPs, and d) $PdAg_2$ NPs. Reaction conditions: 5 μmol total metal on Vulcan CX-72, 5.6 mmol DPA, 20 mL cyclohexane, 8 bar H_2, 35 °C, 1110 rpm.
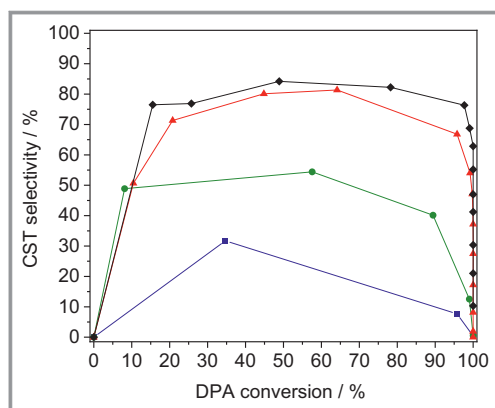
Figure 9. Dependency of the DPA selectivity on DPA conversion for the Pd NPs reference (blue squares), Pd_3Ag NPs (green spheres), PdAg NPs (red triangles), and $PdAg_2$ NPs (black diamonds).

with Ag to reduce surface and strain energy [60]. From a thermodynamic point of view, the atomic arrangement of Ag and Pd in the NPs result from competition between surface segregation effects and chemical ordering tendencies to minimize the free energy. It can be very sensitive to alloy constituents, NP size or shape, and operating conditions due to surface (high surface-to-volume ratio and a number of nonequivalent sites) and finite matter effects (limited

supply of segregation atoms). The energetically favorable composition of Pd-rich Pd_3Ag NPs, for example, was suggested to exhibit a pure Pd-core/mixed-shell structure by segregation of Ag atoms onto the NP surface. The degree of surface segregation is limited by the Ag content of the NPs with Ag atoms preferentially segregating onto lower coordinated sites (such as vertex and edge sites). The core region of the NPs is then depleted in Ag due to this finite matter effect. For $Pd_{0.75}Ag_{0.25}$ NPs (Pd_3Ag) with 9201 atoms (i.e., comparable to the size of our Pd/Ag NPs), the Ag content in the NP core was calculated to 0.1. For liquid-phase hydrogenation of 2-methyl-3-butyn-2-ol over shape-selective Pd catalysts, semi-hydrogenation occurred preferentially at the plane sites regardless their crystallographic orientation, while over-hydrogenation seemed to occur at low coordinated edge sites presumably due to increased adsorption strength of the alkene [63]. Moreover, acetylene hydrogenation reveals an antipathetic structure sensitivity, which also correlates with the increasing fraction of atoms on the facets vs those at the edges and vertices [59]. Preferred Ag segregation at edge and vertice sites of the Pd_3Ag NP surface could also account for the increase in CST yield with respect to our Pd reference NPs, although formation of isolated Pd sites and suppression of Pd hydride phases is not expected for this low Ag content. With increasing total Ag content, the NP structure evolves to a mixed-core/Ag-shell

structure with Pd subsurface for PdAg$_3$ [60]. For Pd/Ag NPs with increased Ag content and equimolar PdAg composition, the segregated Ag atoms seem to not only block the edges, vertices and {100} facets but also isolate Pd ensembles on {111} facets mostly to monomers. Isolated Pd sites have been suggested to limit the capability of the catalyst for over-hydrogenation to DPE. Indeed, the carbon-supported, equimolar PdAg NPs already reveal an increased CST selectivity (67–82 %) up to a DPA conversion of approximately 95 %. Although the CST selectivity further increases with Ag content to 76–84 % in PdAg$_2$ NPs, the effect of Ag alloying seems to be less pronounced above the equimolar PdAg NP composition. The increased Ag content in the NP core of PdAg$_2$ NPs may further reduce formation of PdH$_x$ hydride phases. It should be noted, however, that elemental segregation could not be detected on the basis of the elemental maps by STEM-EDX spectrum imaging (Fig. 5). Eventually, surface segregation behavior may be also modified or even reversed in the presence of strongly binding adsorbates. This should be also taken into account when looking at surface sites by using probes molecules such as CO.

Intermetallic Pd$_2$Sn and PdSn NP catalysts prepared by us using a similar approach in ILs were less active than the bimetallic Pd/Ag NP-derived catalyst but showed comparable CST selectivities in DPA semi-hydrogenation. However, CST was not over-hydrogenated to DPE and CST selectivity did not decrease with reaction time [30]. Both the Sn content and the intermetallic phase seemed to be important in this case. It should be noted that these intermetallic Pd/Sn-based NPs were not supported on carbon and the reaction temperature was also higher (80 °C).

4   Summary and Outlook

In summary, bimetallic Pd/Ag NPs with different Pd/Ag ratios were synthesized in [BMIm][NTf$_2$] at 80 °C using Pd(acac)$_2$ and AgNTf$_2$ as metal precursors and [NBu$_4$][BH$_4$] as a reducing agent. The alloyed Pd/Ag NPs were monodisperse, spherical in shape and well dispersed over the carbon support. The size of the bimetallic Pd/Ag NPs was in a similar size range (4–5 nm) slightly increasing with increasing amount of Ag. In the XRD patterns, insertion of Ag in the Pd fcc lattice and formation of substitutional alloys was indicated by a shift of the 111 reflection to smaller Bragg angles. Moreover, the formation of alloyed NPs was further supported by elemental maps from STEM-EDX spectrum imaging. All catalysts revealed an overall high activity in the semi-hydrogenation of DPA decreasing with Ag content. The CST selectivity and yield improved with increasing Ag content of the NP catalyst. A major increase in CST selectivity and yield was observed up to equimolar PdAg NPs, while the influence of further Ag alloying in PdAg$_2$ NPs seemed to be less pronounced. Theoretical studies on alloyed Pd-Ag NPs previously suggested for NPs with equimolar PdAg composition that segregated Ag atoms not only block the edges, vertices and {100} facets but also isolate Pd ensembles on {111} facets mostly to monomers. Pd site isolation was suggested to improve the catalytic performance in semi-hydrogenation of DPA, which is in good agreement with the catalytic behavior of our model catalysts. In general, synthesis of NPs in ILs provides an interesting approach for the design of model catalysts with varying compositions. Not only the composition of the NPs but also the reaction conditions may be further optimized in future work to increase the overall CST yield in this reaction. Here, also detailed catalytic studies on the influence of the various reaction parameters (such as the metal loading, temperature, pressure and the DPA amount) on the CST/TST selectivity and the yield will be further carried out.

Supporting Information

Supporting Information for this article can be found under DOI: https://doi.org/10.1002/cite.202100163.

Symbols used

2θ	[°]	diffraction angle
r_X	[–]	regression coefficient of compound X
S_P	[%]	selectivity of product P
t	[min]	time
Y_P	[%]	yield of product P

Abbreviations

[BMIm][NTf$_2$]	1-butyl-3-methylimidazolium bis(trifluoromethylsulfonyl)imide
[NBu$_4$][BH$_4$]	tetrabutylammonium borohydride
a.u.	arbitrary units
AgNTf$_2$	silverbis(trifluoromethylsulfonyl)imide
Al$_2$O$_3$	aluminiumoxide
CB	carbon black

CST	*cis*-stilbene
DPA	diphenylacetylene
DPE	1,2-diphenylethane
fcc	face-centered cubic
GC	gas chromatography
hkl	Miller indices
ICDD	International Centre for Diffraction Data
ICP-OES	optical emission spectroscopy with inductively coupled plasma
ILs	ionic liquids
max	maximum
min	minimum
NPs	nanoparticles
OLED	organic light-emitting diode
Pd(acac)$_2$	palladium acetylacetonate
PTFE	polyfluoroethylene
rcf	relative centrifugal force
rpm	rounds per minute
TEM	transmission electron microscopy
THF	tetrahydrofuran
TST	*trans*-stilbene
XRD	powder X-ray diffraction analysis

References

[1] B. Yang, R. Burch, C. Hardacre, G. Headdock, P. Hu, *J. Catal.* **2013**, *305*, 264–276.

[2] A. Borodziński, G. C. Bond, *Catal. Rev.* **2006**, *48 (2)*, 91–144.

[3] J. A. Delgado, O. Benkirane, C. Claver, C. Godard, *Dalton Trans.* **2017**, *46 (37)*, 12381–12403.

[4] M. T. Ravanchi, S. Sahebdelfar, S. Komeili, *React. Chem. Eng.* **2018**, *34 (2)*, 215–237.

[5] Á. Molnár, A. Sárkány, M. Varga, *J. Mol. Catal. A: Chem.* **2001**, *173 (1)*, 185–221.

[6] D. V. Glyzdova, N. S. Smirnova, N. N. Leont'eva, E. Y. Gerasimov, I. P. Prosvirin, V. I. Vershinin, D. A. Shlyapin, P. G. Tsyrul'nikov, *Kinet. Catal.* **2017**, *58 (2)*, 140–146.

[7] *Ionic liquids (ILs) in organometallic catalysis* (Eds: J. Dupont, L. Kollár), Springer, Berlin **2015**.

[8] R. Zhang, Z. Hou, Soluble Pd Nanoparticles for Catalytic Hydrogenation, in *Nanocatalysis in Ionic Liquids* (Ed: M. H. G. Prechtl), Wiley-VCH Verlag, Weinheim **2016**, 83–95.

[9] F. Studt, F. Abild-Pedersen, T. Bligaard, R. Z. Sørensen, C. H. Christensen, J. K. Nørskov, *Science* **2008**, *320 (5881)*, 1320–1322.

[10] A. B. McEwen, M. J. Guttieri, W. F. Maier, R. M. Laine, Y. Shvo, *J. Org. Chem.* **1983**, *48 (23)*, 4436–4438.

[11] M. P. Conley, R. M. Drost, M. Baffert, D. Gajan, C. Elsevier, W. T. Franks, H. Oschkinat, L. Veyre, A. Zagdoun, A. Rossini, M. Lelli, A. Lesage, G. Casano, O. Ouari, P. Tordo, L. Emsley, C. Copéret, C. Thieuleux, *Chem. Eur. J.* **2013**, *19 (37)*, 12234–12238.

[12] T. Mitsudome, Y. Takahashi, S. Ichikawa, T. Mizugaki, K. Jitsukawa, K. Kaneda, *Angew. Chem., Int. Ed.* **2013**, *52 (5)*, 1481–1485.

[13] G. Vilé, N. Almora-Barrios, S. Mitchell, N. López, J. Pérez-Ramírez, *Chem. Eur. J.* **2014**, *20 (20)*, 5926–5937.

[14] P. V. Markov, G. O. Bragina, G. N. Baeva, I. S. Mashkovskii, A. V. Rassolov, I. A. Yakushev, M. N. Vargaftik, A. Y. Stakheev, *Kinet. Catal.* **2016**, *57 (5)*, 625–631.

[15] C. W. A. Chan, A. H. Mahadi, M. M.-J. Li, E. C. Corbos, C. Tang, G. Jones, W. C. H. Kuo, J. Cookson, C. M. Brown, P. T. Bishop, S. C. E. Tsang, *Nat. Commun.* **2014**, *5 (1)*, 5787.

[16] V. R. Naina, S. Wang, D. I. Sharapa, M. Zimmermann, M. Hähsler, L. Niebl-Eibenstein, J. Wang, C. Wöll, Y. Wang, S. K. Singh, F. Studt, S. Behrens, *ACS Catal.* **2021**, *11 (4)*, 2288–2301.

[17] W. Niu, Y. Gao, W. Zhang, N. Yan, X. Lu, *Angew. Chem., Int. Ed.* **2015**, *54 (28)*, 8271–8274.

[18] G. Vilé, N. Almora-Barrios, S. Mitchell, N. López, J. Pérez-Ramírez, *Chem. Eur. J.* **2014**, *20 (20)*, 5849–5849.

[19] M. Tejeda-Serrano, J. R. Cabrero-Antonino, V. Mainar-Ruiz, M. López-Haro, J. C. Hernández-Garrido, J. J. Calvino, A. Leyva-Pérez, A. Corma, *ACS Catal.* **2017**, *7 (5)*, 3721–3729.

[20] Z. Wang, L. Yang, R. Zhang, L. Li, Z. Cheng, Z. Zhou, *Catal. Today* **2016**, *264*, 37–43.

[21] A. V. Rassolov, G. O. Bragina, G. N. Baeva, I. S. Mashkovsky, A. Y. Stakheev, *Kinet. Catal.* **2020**, *61 (6)*, 869–878.

[22] V. V. Chesnokov, A. S. Chichkan, Z. R. Ismagilov, *Kinet. Catal.* **2017**, *58 (5)*, 649–654.

[23] K. Wang, G. Li, C. Wu, X. Sui, Q. Wang, J. He, *J. Cluster Sci.* **2016**, *27 (1)*, 55–62.

[24] P. Concepción, S. García, J. C. Hernández-Garrido, J. J. Calvino, A. Corma, *Catal. Today* **2016**, *259*, 213–221.

[25] M. Armbrüster, K. Kovnir, M. Behrens, D. Teschner, Y. Grin, R. Schlögl, *J. Am. Chem. Soc.* **2010**, *132 (42)*, 14745–14747.

[26] M. Armbrüster, G. Wowsnick, M. Friedrich, M. Heggen, R. Cardoso-Gil, *J. Am. Chem. Soc.* **2011**, *133 (23)*, 9112–9118.

[27] I. S. Mashkovsky, P. V. Markov, G. O. Bragina, G. N. Baeva, A. V. Rassolov, I. A. Yakushev, M. N. Vargaftik, A. Y. Stakheev, *Nanomat.* **2018**, *8 (10)*, 769.

[28] Y. Luo, S. Alarcón Villaseca, M. Friedrich, D. Teschner, A. Knop-Gericke, M. Armbrüster, *J. Catal.* **2016**, *338*, 265–272.

[29] M. Neumann, D. Teschner, A. Knop-Gericke, W. Reschetilowski, M. Armbrüster, *J. Catal.* **2016**, *340*, 49–59.

[30] C. Dietrich, S. Chen, G. Uzunidis, M. Hähsler, Y. Träutlein, S. Behrens, *ChemistryOpen* **2021**, *10 (2)*, 296–304.

[31] S. Furukawa, T. Komatsu, *ACS Catal.* **2016**, *6 (3)*, 2121–2125.

[32] I. G. Aviziotis, A. Götze, F. Göhler, H. Kohlmann, M. Armbrüster, *Z. Anorg. Allg. Chem.* **2018**, *644 (24)*, 1777–1781.

[33] O. Matselko, R. R. Zimmermann, A. Ormeci, U. Burkhardt, R. Gladyshevskii, Y. Grin, M. Armbrüster, *J. Phys. Chem. C* **2018**, *122 (38)*, 21891–21896.

[34] O. Matselko, U. Burkhardt, Y. Prots, R. R. Zimmermann, M. Armbrüster, R. Gladyshevskii, Y. Grin, *Eur. J. Inorg. Chem.* **2017**, *2017 (29)*, 3542–3550.

[35] R. K. Rai, M. K. Awasthi, V. K. Singh, S. R. Barman, S. Behrens, S. K. Singh, *Catal. Sci. Technol.* **2020**, *10 (15)*, 4968–4980.

[36] K. Schütte, A. Doddi, C. Kroll, H. Meyer, C. Wiktor, C. Gemel, G. van Tendeloo, R. A. Fischer, C. Janiak, *Nanoscale* **2014**, *6 (10)*, 5532–5544.

[37] M. Armbrüster, K. Kovnir, M. Friedrich, D. Teschner, G. Wowsnick, M. Hahne, P. Gille, L. Szentmiklósi, M. Feuerbacher, M. Heggen, F. Girgsdies, D. Rosenthal, R. Schlögl, Y. Grin, *Nat. Mater.* **2012**, *11 (8)*, 690–693.

[38] B. Bridier, J. Pérez-Ramírez, *J. Am. Chem. Soc.* **2010**, *132 (12)*, 4321–4327.

[39] G. X. Pei, X. Y. Liu, A. Wang, A. F. Lee, M. A. Isaacs, L. Li, X. Pan, X. Yang, X. Wang, Z. Tai, K. Wilson, T. Zhang, *ACS Catal.* **2015**, *5 (6)*, 3717–3725.

[40] M. Armbrüster, M. Behrens, F. Cinquini, K. Föttinger, Y. Grin, A. Haghofer, B. Klötzer, A. Knop-Gericke, H. Lorenz, A. Ota, S. Penner, J. Prinz, C. Rameshan, Z. Révay, D. Rosenthal, G. Rupprechter, P. Sautet, R. Schlögl, L. Shao, L. Szentmiklósi, D. Teschner, D. Torres, R. Wagner, R. Widmer, G. Wowsnick, *ChemCatChem* **2012**, *4 (8)*, 1048–1063.

[41] D. C. Huang, K. H. Chang, W. F. Pong, P. K. Tseng, K. J. Hung, W. F. Huang, *Catal. Lett.* **1998**, *53 (3)*, 155–159.

[42] D. Mei, M. Neurock, C. M. Smith, *J. Catal.* **2009**, *268 (2)*, 181–195.

[43] S. González, K. M. Neyman, S. Shaikhutdinov, H.-J. Freund, F. Illas, *J. Phys. Chem. C* **2007**, *111 (18)*, 6852–6856.

[44] T. Mitsudome, T. Urayama, K. Yamazaki, Y. Maehara, J. Yamasaki, K. Gohara, Z. Maeno, T. Mizugaki, K. Jitsukawa, K. Kaneda, *ACS Catal.* **2016**, *6 (2)*, 666–670.

[45] K. Kakaei, M. Dorraji, *Electrochim. Acta* **2014**, *143*, 207–215.

[46] W. Hong, J. Wang, E. Wang, *Electrochem. Commun.* **2014**, *40*, 63–66.

[47] D. A. Slanac, W. G. Hardin, K. P. Johnston, K. J. Stevenson, *J. Am. Chem. Soc.* **2012**, *134 (23)*, 9812–9819.

[48] D. I. Sharapa, D. E. Doronkin, F. Studt, J.-D. Grunwaldt, S. Behrens, *Adv. Mater.* **2019**, *31 (26)*, 1807381.

[49] I. Karakaya, W. T. Thompson, *Bull. Alloy Phase Diagrams* **1988**, *9 (3)*, 237–243.

[50] L. Yang, Y. Wang, H. Feng, H. Zeng, C. Tan, J. Yao, J. Zhang, L. Jiang, Y. Sun, *Chem. Asian J.* **2021**, *16 (1)*, 34–38.

[51] S. Zhang, Ö. Metin, D. Su, S. Sun, *Angew. Chem., Int. Ed.* **2013**, *52 (13)*, 3681–3684.

[52] Z. Yin, Y. Zhang, K. Chen, J. Li, W. Li, P. Tang, H. Zhao, Q. Zhu, X. Bao, D. Ma, *Sci. Rep.* **2014**, *4 (1)*, 4288.

[53] C. Feldmann, M. Ruck, *Z. Anorg. Allg. Chem.* **2017**, *643 (1)*, 2–2.

[54] E. Ahmed, J. Breternitz, M. F. Groh, M. Ruck, *CrystEngComm* **2012**, *14 (15)*, 4874–4885.

[55] C. Dietrich, M. Hähsler, W. Wang, C. Kübel, S. Behrens, *ChemNanoMat* **2020**, *6 (12)*, 1854–1862.

[56] C. Dietrich, G. Uzunidis, Y. Träutlein, S. Behrens, *JoVE* **2018**, *138*, e58058.

[57] C. Dietrich, D. Schild, W. Wang, C. Kübel, S. Behrens, *Z. Anorg. Allg. Chem.* **2017**, *643 (1)*, 120–129.

[58] S. Essig, S. Behrens, *Chem. Ing. Tech.* **2015**, *87 (12)*, 1741–1747.

[59] P. V. Markov, I. S. Mashkovsky, G. O. Bragina, J. Wärnå, V. I. Bukhtiyarov, A. Y. Stakheev, D. Y. Murzin, *Chem. Eng. J.* **2021**, *404*, 126409.

[60] J. Tang, L. Deng, H. Deng, S. Xiao, X. Zhang, W. Hu, *J. Phys. Chem. C* **2014**, *118 (48)*, 27850–27860.

[61] A. V. Rassolov, D. S. Krivoruchenko, M. G. Medvedev, I. S. Mashkovsky, A. Y. Stakheev, I. V. Svitanko, *Mendeleev Commun.* **2017**, *27 (6)*, 615–617.

[62] A. V. Rassolov, P. V. Markov, G. O. Bragina, G. N. Baeva, I. S. Mashkovskii, I. A. Yakushev, M. N. Vargaftik, A. Y. Stakheev, *Kinet. Catal.* **2016**, *57 (6)*, 853–858.

[63] M. Crespo-Quesada, A. Yarulin, M. Jin, Y. Xia, L. Kiwi-Minsker, *J. Am. Chem. Soc.* **2011**, *133 (32)*, 12787–12794.